



Modest modulation on the electronic structure of Co₉S₈ by vanadium doping for high-performance rechargeable Zn–air batteries

Lin Wu^a, Shuxin Li^a, Lixiang Li^{a,b,**}, Han Zhang^{a,*}, Lin Tao^a, Xin Geng^{a,b}, Haiming Yang^{a,b}, Weimin Zhou^{a,b}, Chengguo Sun^{a,c}, Dongying Ju^b, Baigang An^{a,b,**}

^a Key Laboratory of Energy Materials and Electrochemistry Research Liaoning Province, School of Chemical Engineering, University of Science and Technology Liaoning, Anshan 114051, China

^b Hainan Provincial Key Lab of Fine Chemistry, School of Chemical Engineering and Technology, Hainan University, Haikou 570228, China

^c School of Chemical Engineering, Nanjing University of Science and Technology, Nanjing 210094, China

ARTICLE INFO

Keywords:

Vanadium doping
Spin state transition
Oxygen reduction reaction
Oxygen evolution reaction
Zn-air battery

ABSTRACT

Rechargeable Zn-air batteries (ZABs) have been attracting research interests worldwide owing to their high energy density, as well as the good safety and low cost. However, the lack of highly active bifunctional electrocatalysts for oxygen reduction reaction (ORR) and oxygen evolution reaction (OER) at air cathode seriously hinders its developments. Herein, a vanadium doped Co₉S₈ (V-Co₉S₈) nanoparticles encapsulated in the nitrogen-doped porous carbon nanoflowers (NFs) has been prepared by an innovative double-solvent approach (DSA) that can precisely control the level of vanadium doping. The magnetic measurements and the theoretical calculation consistently demonstrate that the spin state of Co can be optimized by tuning the vanadium doping level. The spin-state modulation raises the *d*-band center of Co and enables the enhanced Co-S covalency in V-Co₉S₈, which balances the adsorption/desorption of oxygen intermediates and finally accelerates the oxygen redox kinetic. As a result, V-Co₉S₈ serving as a cost-effectively bifunctional catalyst for the cathode of a rechargeable ZAB, supplies a superb power density of 345 mW cm⁻², an energy density of 814 mAh g_{Zn}⁻¹ and a super durability with a stable operation of 840 cycles, which outperforms the noble metal catalyst (Pt/C and RuO₂) and the most Co based catalysts reported recently.

1. Introduction

Reversible electrocatalysis toward the oxygen reactions plays a key role on the advanced systems for conversion and storage of clean and sustainable energy, such as fuel cells [1], metal-air batteries and electrolyzers [2,3]. Among these systems, rechargeable Zn-air batteries (ZABs) are highly potential due to the inherent safety and the natural abundance of the materials, as well as the highly theoretical energy density (1086 Wh kg⁻¹) [4]. The oxygen evolution reaction (OER) and the oxygen reduction reaction (ORR) are the keys to complete the mutual conversion of electrical energy and chemical energy of ZABs. As both ORR and OER suffer from the intrinsically sluggish kinetics, advanced electrocatalysts are requisite to ensure the efficiency of ZABs [5–10]. Although the precious metals (compounds) of Pt, Ir, RuO₂, etc., own the high activity on ORR or OER [11–13], whereas their severe

scarcity, insufficient bifunctionality and unsatisfying stability have seriously limited their developments and applications. Therefore, the intensive researches are paying on developing the cost-effective and robust alternatives [14,15].

Great progresses have been achieved on the development of non-noble metal-based electrocatalysts for both ORR and OER, such as metal oxides [16], sulfides [17,18], phosphides, and nitrides [19–21]. Among them, cobalt sulfide (Co₉S₈) is regarded as an attractive electrocatalyst due to its highly catalytic activity and excellent electrochemical stability. In comparison to bulk Co₉S₈, nanostructured Co₉S₈ catalysts could afford more active sites and the faster transfer rate of ions/electrons during the electrocatalytic reaction, and thus exhibit the enhanced ORR and OER activity [22–25]. A variety of Co₉S₈ (e.g., nanoparticles [26] and nanospheres [27]) and their composites (Co₉S₈ embedded into N/S-doped carbon composites [28], Co₉S₈@NiCo₂O₄

* Corresponding author.

** Corresponding authors at: Key Laboratory of Energy Materials and Electrochemistry Research Liaoning Province, School of Chemical Engineering, University of Science and Technology Liaoning, Anshan 114051, China.

E-mail addresses: lxli2005@126.com (L. Li), hzhang0807@163.com (H. Zhang), bgan@ustl.edu.cn (B. An).

<https://doi.org/10.1016/j.apcatb.2022.122250>

Received 3 July 2022; Received in revised form 8 October 2022; Accepted 30 November 2022

Available online 5 December 2022

0926-3373/© 2022 Elsevier B.V. All rights reserved.

nanobrushes [29] and fiber-in-tube Co₉S₈-Carbon [30]) have been designed from the aspects of the nanostructures, the heteroatoms doping, the heterostructures and the composite structure with nano-carbon to demonstrate their advances on improving the performance toward ORR and OER as catalysts. It makes Co₉S₈ based catalyst a promising family for application in ZABs.

To further develop Co₉S₈ based catalyst family, it is necessary to insight what interrelates the intrinsic activity and how it influences the property of catalyst. As is known, the d orbitals of transition metal atoms are the activity sources of catalysts, the d-band electronic configuration becomes one critical aspect to optimize the property of catalysts. According to the d-band center theory [31–34], the movement of d-band close to the Fermi level (E_F) leads to the less occupation of the anti-bonding states (anti-bonding states occupation is related to spin state) corresponding to the stronger adsorption of intermediates. Thus, the tailoring d-band position performs as an efficient approach to optimize the performance of catalyst. The recent studies have shown that the d-band center (E_d) energy level positions of Co₃O₄, LaCoO₃ and Co₄N affecting the spin state can be tailored via the metal atoms replacement [35–37], suggesting that the spin state and the E_d energy level modulation are effective methods to accelerate the ORR/OER. Therefore, modulating the E_d energy level and the spin state of Co active site would be valuable to promote the intrinsic activity of Co₉S₈ catalysts.

Vanadium owns abundant vacant d-orbitals and thus is one of ideal candidates to regulate the spin state and the E_d energy level of Co₉S₈. Herein, the vanadium-doped Co₉S₈ (V-Co₉S₈) nanoparticles encapsulated in nitrogen-doped porous carbon nanoflowers (NFs) has been prepared by an innovative double-solvent approach (DSA). The resulted V-Co₉S₈ by the modest vanadium doping shows the significantly enhanced property toward ORR and OER. The magnetic measurements and the theoretical calculations unveil that V-substituted Co ion sites make the spin state of Co₉S₈ transit from high spin to modest spin state to raise d-band center, indicating that the antibonding orbital is pushed up by Co d_{z^2} . The spin-state modulation of V-Co₉S₈ enables the enhanced Co-S covalency in V-Co₉S₈, which balances the adsorption/desorption of oxygen intermediates. Consequently, the V-Co₉S₈ displays a superior ability catalyzing the ORR (0.83 V, half-wave potential) and the OER (0.38 V at 10 mA cm⁻², overpotential). As the bifunctional catalyst, the rechargeable ZAB with V-Co₉S₈ shows an excellent overall performance of a high-power density (345 mW cm⁻²), a high specific capacity (814 mAh g_{Zn}⁻¹, about 99.3% of the theoretical capacity) and a super cycling stability over 840 cycles. All the properties are superior than the noble metal catalyst and the most Co based catalysts recently reported [38–41].

2. Experimental section

2.1. Synthesis of NH₂-MIL-101(Al)

NH₂-MIL-101(Al) precursor was synthesized as the previous reports [42]. In a typical synthesis, 2-aminoterephthalic acid (4.15 g, 23 mmol) and N, N-dimethylformamide (DMF, 1000 mL) were first mixed in 2000 mL round bottom flask and heated to 110 °C in an oil bath. Then, AlCl₃·6H₂O (11.06 g, 46 mmol) was added in seven equal portions, every addition interval 15 min. After the last portion was added, the temperature was kept at 110 °C for 3 h under stirring and for an additional 16 h without stirring. After cooling down to room temperature, the yellow faint solid was separated by centrifugation, washed with DMF and ethanol for three times, and then further purified by treatment in ethanol at 90 °C for 16 h. The yellow faint solid was finally collected and dried at 120 °C for 12 h under vacuum.

2.2. Encapsulation of vanadium trichloride and cobalt-sulfur compound into NH₂-MIL-101(Al)

The vanadium trichloride and cobalt-sulfur compound were

encapsulated into the pores of NH₂-MIL-101(Al) by a double-solvent approach (DSA). 500 mg of NH₂-MIL-101(Al) was suspended in 100 mL of hydrophobic n-hexane, and sonicated for about half an hour to make the mixture homogenously. Afterwards, 0.7 mL of water-methanol hydrophilic solution containing vanadium trichloride (0, 2, 5 and 10 mg), thiourea (100 mg) and cobalt chloride (100 mg) compound were added dropwisely into hydrophobic n-hexane solution. After stirring for 3 h, the product was dried at 120 °C for 12 h, leading to the formation of Co@NH₂-MIL-101(Al) and V-Co@NH₂-MIL-101(Al).

2.3. Synthesis of nanoflowers V-Co₉S₈ catalysts

The as-prepared Co@NH₂-MIL-101(Al) and V-Co@NH₂-MIL-101(Al) were annealed at 800 °C for 5 h at a heating ramp of 5 °C min⁻¹ in a tube furnace with an argon flow. The residual Al component and other impurities were removed by immersing the samples in the HF (20 wt%) solution for 36 h. The black powder materials were collected by centrifuging, washing several times with plenty of distilled water, and drying at 120 °C under vacuum for 12 h. The resulting samples were denoted as Co₉S₈ and V-Co₉S₈-X, where X is the amount of vanadium trichloride encapsulated.

2.4. Structure Characterization

The crystal structure, morphology and surface area of the products were characterized by X-ray diffraction (XRD, D/MAX-2500X), Raman spectra (Raman, Xplora Plus), scanning electron microscopy (SEM, Thermo Fisher Scientific Apreos), transmission electron microscopy (TEM, FEI Tecnai G2 F30, JEM ARM 200 F) and Brunner-Emmet-Teller (BET, ASAP2020 Micromeritics). The composition, elemental analysis and valence electron structure were analyzed by X-ray photoelectron spectroscopy (XPS, ASIS SUPRA), inductively coupled plasma atomic emission spectrometry (ICP, Agilent ICPAES730), elemental analyzer (EA, LECO ONH863), ultraviolet photoelectron spectroscopy (UPS, ASIS SUPRA) and electron paramagnetic resonance (EPR, A300–10/12). The magnetic measurements were carried out with a MPMS SQUID magnetometer.

2.5. Electrochemical measurements

The electrochemical measurements were performed on CHI660E electrochemical workstation through a standard three-electrode system. The glassy carbon (GC) electrode (diameter of 4 mm with surface area of 0.13 cm²) coated with catalyst layer was used as a working electrode (WE), while a Pt foil was used as counter electrode (CE). Hg/HgO was used as a reference electrode (RE). The Potential value of Hg/HgO electrode was all converted to corresponding standards reversible hydrogen electrode (RHE) according to Nernst equation. 5 mg catalysts were dispersed in a mixture of deionized water (500 μL), ethanol (500 μL) and Nafion (50 μL, 5 wt%) to form a uniform catalyst ink. The catalyst ink was then spinning drop-casted (<700 rpm) onto the GC electrode with a 0.24 mg cm⁻² loading for all samples. Both the ORR and OER of samples were tested in 0.1 M KOH /1 M KOH solution saturated with oxygen. Before CV and LSV tests, the working electrodes were activated by CV test at a scan rate of 50 mV s⁻¹ for several times.

The LSV tests were performed at a scan rate of 10 mV s⁻¹. For the ORR tests, the WE was scanned cathodically at a rate of 10 mV s⁻¹ with the rotating speed from 400 to 2500 rpm in O₂-saturated 0.1 M KOH aqueous solution. EIS measurements were carried out by applying an AC voltage with 5 mV amplitude in a frequency range from 100 kHz to 100 mHz in 1 M KOH solution. The electron transfer number (n) of ORR was calculated from the Koutecky-Levich equation [43]:

$$\frac{1}{j} = \frac{1}{j_L} + \frac{1}{j_K} = \frac{1}{B\omega^{0.5}} + \frac{1}{j_K}$$

$$B = 0.62nFC_{O_2}(D_{O_2})^{2/3}\nu^{-1/6}$$

$$J_K = nFkC_0$$

$$F=96485\text{ C mol}^{-1}, D_{O_2}=1.9\times 10^{-5}\text{ cm}^2\text{ s}^{-1}, \nu=0.01\text{ cm}^2\text{ s}^{-1}, \\ C_{O_2}=1.2\times 10^{-6}\text{ mol cm}^{-3}.$$

From the Koutecky-Levich equation, we can get the kinetic current density j_K , and the slope of the linear plot of logarithmic j_K to overpotential is the Tafel slope. The ECSA was calculated from the electric double layer capacitance (C_{dl}) measured in a potential window without Faradaic response. A series of measured CV curves at scanning rates of 10, 20, 30, 40 and 50 mV s^{-1} , and the potential range from 0.95 to 1.05 V vs. RHE. The C_{dl} was estimated by plotting the variance between anodic and cathodic current ($\Delta j = j_a - j_c$) against the scan rates. The slope of the linear fitting line was twice of the C_{dl} value, which is proportional to the ECSA of the resulting catalysts.

2.6. Preparation of rechargeable Zn-air batteries

The rechargeable Zn-air batteries (ZABs) were tested by a two electrode system in 6.0 M KOH aqueous electrolyte with 0.2 M $\text{Zn}(\text{Ac})_2$. The as-prepared catalyst ink was attached to carbon fiber paper to form the air electrode (load capacity $\approx 0.3\text{ mg cm}^{-2}$). The polished Zn plate (0.2 mm thickness) was served as anode.

2.7. Density functional theory (DFT) calculations

First-principles calculations were performed within the density functional theory (DFT) framework [44]. The projector-augmented wave (PAW) method and the generalized gradient approximation (GGA) for the exchange-correlation energy functional, as implemented in the Vienna Ab initial Simulation Package (VASP) were used. The GGA calculation was carried out with the Perdew-Burke-Ernzerhof (PBE) exchange-correlation potential. The Van der Waals interactions were considered in hetero-structure models using DFT-D correlation [45]. The vacuum space was set as 20 Å to avoid effects of periodic slabs. The convergence criterion of geometry relaxation was set to 0.01 eV/Å in force on each atom. A 2×2 supercell of the Co_9S_8 (311) and CoOOH (001) surface including 8 at. layer were constructed to model the catalyst in this work. The primitive models of Co_9S_8 and CoOOH were used to construct band structure. The energy cutoff for plane wave-basis was set to 500 eV. The K-points were sampled with $2 \times 2 \times 1$ by Monkhorst-Pack method.

For OER, the Gibbs free energy was calculated by the generally reported four electrons process:



where * represents an adsorption site on the catalyst, and $*\text{OH}$, $*\text{O}$ and $*\text{OOH}$ denote the corresponding adsorbed intermediates. Also, at standard conditions, the free energies change for all OER electrochemical steps (ΔG_{1-4}) can be expressed as:

$$\Delta G_1 = \Delta G_{*\text{OH}} \quad (5)$$

$$\Delta G_2 = \Delta G_{*\text{O}} - \Delta G_{*\text{OH}} \quad (6)$$

$$\Delta G_3 = \Delta G_{*\text{OOH}} - \Delta G_{*\text{O}} \quad (7)$$

$$\Delta G_4 = 4.92 - \Delta G_{*\text{OOH}} \quad (8)$$

Therefore, the theoretical overpotential η was obtained according to the equation:

$$\eta = \max[\Delta G_1, \Delta G_2, \Delta G_3, \Delta G_4]/e - 1.23\text{ V} \quad (9)$$

The change in free energy (ΔG) of per reaction step was calculated as following [46]:

$$\Delta G = \Delta E + \Delta \text{ZPE} - T \cdot \Delta S + \Delta G_U + \Delta G_{\text{pH}} \quad (10)$$

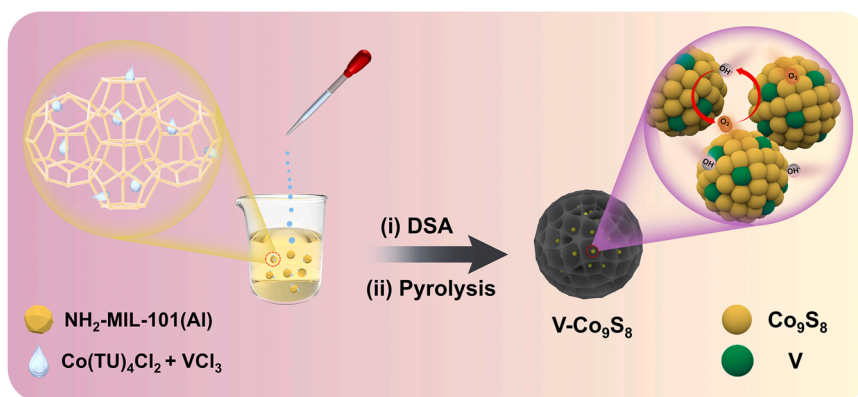
where ΔE is the change of the total reaction energy obtained from DFT calculation, ΔZPE is the change of the zero-point energy, T is the temperature (300 K), and ΔS is the change of the entropy. $\Delta G_U = -eU$, where U is the potential at the electrode and e is the transferred charge. $\Delta G_{\text{pH}} = k_B \cdot T \times \ln 10 \times \text{pH}$, where k_B is the Boltzmann constant and $T = 300\text{ K}$. In this work, the influence of pH was neglected. The free energy of O_2 is obtained from the reaction $\text{O}_2 + 2\text{H}_2 \rightarrow 2\text{H}_2\text{O}$, which is 4.92 eV at 300 K and pressure of 0.035 bar. The free energy of OH^- is defined as $G(\text{H}_2\text{O}) - G(\text{H}^+)$, and the free energy of H^+ is equal to $1/2\text{ H}_2$. The entropies of molecules (including O_2 , H_2 and H_2O , etc.) in the gas (or liquid) phase are taken from the "CRC Handbook of Chemistry and Physics".

3. Results and discussion

3.1. Synthesis and characterization of the V- Co_9S_8

Scheme 1 illustrates the synthetic process of vanadium-doped Co_9S_8 (V- Co_9S_8) nanoparticles confined in nitrogen-doped porous carbon nanoflowers by DSA. Firstly, the uniform nanocrystals of $\text{NH}_2\text{-MIL-101}(\text{Al})$ were fabricated by coordinating Al^{3+} with 2-aminoterephthalic acid in DMF (Fig. 1a). The $\text{NH}_2\text{-MIL-101}(\text{Al})$ as prepared has a high specific surface areas ($2859\text{ m}^2\text{ g}^{-1}$) and each $\text{NH}_2\text{-MIL-101}(\text{Al})$ molecular has two large hydrophilic cavities (2–3 nm in diameter) with the windows size of (1.2 and 1.6 nm) (Fig. S1). Secondly, the DSA based on the immiscibility of a hydrophilic solvent (methanol-water solution of $\text{Co}(\text{Tu})_4\text{Cl}_2$ and VCl_3) and a hydrophobic solvent (n-hexane suspension of $\text{NH}_2\text{-MIL-101}(\text{Al})$) was applied [47]. The droplets of $\text{Co}(\text{Tu})_4\text{Cl}_2$ and VCl_3 aqueous solution added to the n-hexane would disperse into numerous droplets under vigorous stirring, and then diffuses into the hydrophilic pores of the $\text{NH}_2\text{-MIL-101}(\text{Al})$ suspended in hydrophobic n-hexane. The aqueous $\text{Co}(\text{Tu})_4\text{Cl}_2$ and VCl_3 guests could be enclosed into the hydrophilic nanopores by the capillary action and the hydrophilic groups, which makes the solid material change from light yellow to green (Fig. 1b). In the DSA, the molecular diameter of the hydrophilic $\text{Co}(\text{Tu})_4\text{Cl}_2$ and the VCl_3 are 7.36 Å and 3.12 Å, which are both smaller than the pore of the adsorbent of $\text{NH}_2\text{-MIL-101}(\text{Al})$, they can uniformly and totally go inside the hydrophilic pores. It can be confirmed by the transmission electron microscope (TEM) observation that the color inside the poured samples became significantly darker (Fig. S2). Moreover, the appreciable decreases in the specific surface areas and the pore volumes of V- $\text{Co}@\text{NH}_2\text{-MIL-101}(\text{Al})$ indicate that the pores of the $\text{NH}_2\text{-MIL-101}(\text{Al})$ framework are occupied by the cobalt compound (Fig. S3 and Table S1). There are no obvious differences in the morphology between the $\text{NH}_2\text{-MIL-101}(\text{Al})$ and the V- $\text{Co}@\text{NH}_2\text{-MIL-101}(\text{Al})$ according to the scanning electron microscopy (SEM) images as shown in Fig. S4, suggesting that the preparing processes does not cause the structure damage.

The XRD patterns of samples are shown in Fig. S5. The diffraction peak intensity of V- $\text{Co}@\text{NH}_2\text{-MIL-101}(\text{Al})$ framework becomes weak and no significant diffraction peaks of Co and V can be detected. During pyrolysis of the V- $\text{Co}@\text{NH}_2\text{-MIL-101}(\text{Al})$ composite to get the V- Co_9S_8 , a large amount of N and S containing gases could be released according to the reaction (Fig. S6) to produce a substantial amount of the internal stresses and strains in the $\text{NH}_2\text{-MIL-101}(\text{Al})$ framework, resulting the unique nanoflowers structure with average particle size of about 500 nm (Fig. 1c). The Co_9S_8 nanoparticles (30–60 nm) are uniformly confined in the petals of carbon NFs (Fig. 1d). Due to the nanopore confinement effect, the severe shrinkage and aggregation of Co_9S_8 nanoparticles can be avoided [48]. The unique and open NFs could not only favor



Scheme 1. Schematic illustration of vanadium doped Co_9S_8 nanoparticles ($\text{V-Co}_9\text{S}_8$) confined in nanoflowers structure.

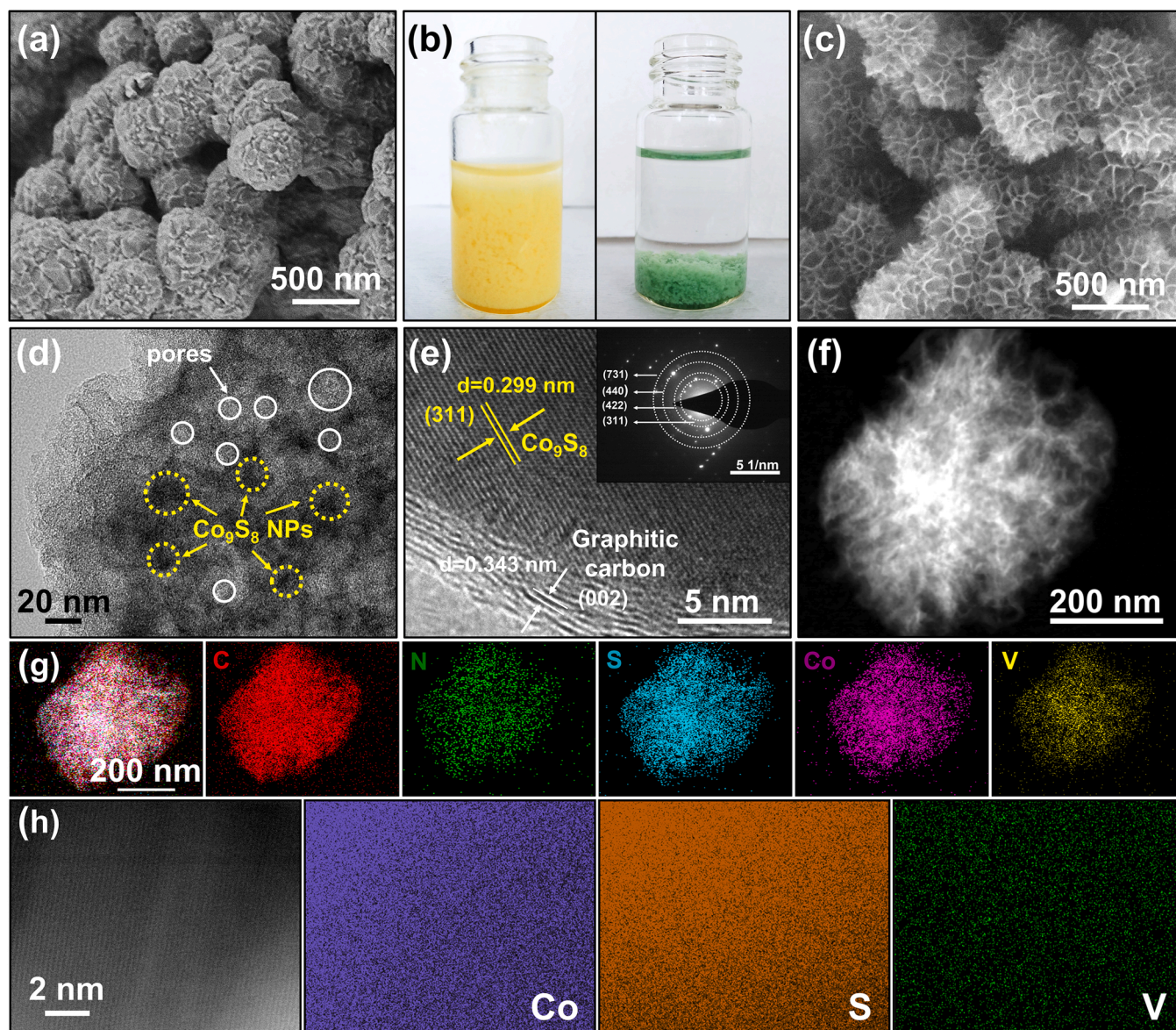


Fig. 1. SEM images of (a) $\text{NH}_2\text{-MIL-101(Al)}$ and (c) $\text{V-Co}_9\text{S}_8$. (b) A digital photograph $\text{NH}_2\text{-MIL-101(Al)}$ (yellow) and $\text{V-Co@NH}_2\text{-MIL-101(Al)}$ (green). (d) TEM and (e) HR-TEM images of the $\text{V-Co}_9\text{S}_8$; the inset shows the selected area electron diffraction (SAED) pattern. (f-g) HAADF-STEM image of $\text{V-Co}_9\text{S}_8$ and the corresponding elemental mapping of C, N, S, Co and V. (h) Elemental mapping of Co, S and V (scale bars, 2 nm).

promoting the homogeneous active sites but also serve as a buffering reservoir to shorten the diffusion distances of the electrolyte toward the active sites [49]. Meanwhile, the V-Co₉S₈ morphology changes slightly with the vanadium doping amount (Fig. S7).

As shown in Fig. 1e, high resolution transmission electron microscopy (HR-TEM), demonstrates the lattice spaces of 0.299 and 0.344 nm indexed to (311) plane of Co₉S₈ NPs and the (002) plane of the graphitic carbon layers [50]. The Co₉S₈ NPs presents a cubic phase crystalline as shown by the selected area electron diffraction (inset of Fig. 1e). Such the structure of Co₉S₈ confined in the graphitic carbon layers could enhance the electron transport and suppress the dissolution and agglomeration of Co₉S₈ NPs, thereby promoting the electrochemical activity and stability of catalyst [51]. As shown in Fig. 1f-g, the C, N, S, Co and V elements distribute uniformly across the entire samples, while V, Co and S ions exist dominantly within the nanoflowers. The sub-nanometer spatial resolution energy-dispersive X-ray spectroscopic (EDS) analysis was performed to clarify the spatial elements distribution in V-doped Co₉S₈. A uniform distribution of V elements at nearly atomic level can be observed (Fig. 1h). This finding is consistent with our novel double-solvent approach strategy and nanopore confinement effect that Co ions are readily replaced with V ions. According to the inductively coupled plasma and elemental analysis, the average weight content of Co, S, and V in the V-Co₉S₈ was 5.85%, 7.15%, and 0.26% (Table S2). The results suggest that the uniform encapsulation of guests within the NH₂-MIL-101(Al) framework could not only make the gas released by the decomposition of the guest molecules to form a unique nanoflower architecture, but also facilitate the uniform doping of vanadium in Co₉S₈ due to the pore confinement effect.

As shown in Fig. 2a and Fig. S8, the XRD patterns of Co₉S₈ are well indexed to cubic phase Co₉S₈ [JCPDS No.19-0364, space group: Fm $\bar{3}$ m (225), $a = b = c = 9.9273$ Å]. The diffraction peak of V-Co₉S₈ positively shifts a little compared to that of Co₉S₈. According to the Bragg's equation, this positive shift of the diffraction peaks corresponds to the decrease of the interlayer distance. Therefore, such a reduction of the lattice distance indicates the tighter packing of the crystal plane [52], ascribing to that Co²⁺ (0.75 Å) is partially substituted by V⁴⁺ (0.58 Å) or V³⁺ (0.64 Å) with the smaller ion radius [53], which is similar to some

cases seen in cation-doped cobalt compounds [54]. The vanadium doping also makes the E_g and A_{1g} characteristic peaks of V-Co₉S₈ shift to 428 cm⁻¹ and 553 cm⁻¹ comparing with Co₉S₈ of 443 cm⁻¹ and 566 cm⁻¹ [55,56] (Fig. 2b). The reason of peaks shift is the increase of van der Waals force between the Co₉S₈ layers caused by the decrease of interlayer spacing due to the vanadium doping, which would result in the weaker out-of-plane vibration [57]. Nitrogen-adsorption/desorption experiments were further performed to investigate the effect of vanadium introduction on material porosity (Fig. 2c and Table S1). Both V-Co₉S₈ and Co₉S₈ show the type-IV isotherms [58], indicating their microporous and mesoporous structures, which is further confirmed by the corresponding distribution of micropores and mesopores (Fig. S9). The V-Co₉S₈ owns the higher specific surface area (1059 m² g⁻¹) and the larger pore volume (0.89 cm³ g⁻¹) than the Co₉S₈ (867 m² g⁻¹ and 0.82 cm³ g⁻¹). It could be attributed to that the decomposition of vanadium trichloride generate chlorine-containing gas during pyrolysis resulting in the increase of micropores and the specific surface area.

The elements of C, N, S and Co are present in Co₉S₈ and V-Co₉S₈ samples and the successful V-doping can be confirmed by comparing the XPS survey spectra of Co₉S₈ and V-Co₉S₈ (Fig. S10a and Table S2). The presence of C and N elements originates from the N-doped porous carbon nanoflowers (Fig. S10b and Fig. S11a). The high-resolution S 2p spectrum is composed of three peaks as shown in Fig. 2d and Fig. S11b, in which the peaks at 164.5 and 163.3 eV are assigned to C=S and C-S of the NFs. Another peak at 161.5 eV is ascribed to the cobalt-sulfur bonding species in Co₉S₈ and V-Co₉S₈ [59]. The high-resolution V 2p spectra verify that vanadium is successfully doped in Co₉S₈ and exists as V³⁺ and V⁴⁺ (Fig. 2e and Fig. S11c). In the high-resolution Co 2p spectra (Fig. 2f), the peaks around the binding energy of 778.5 eV and 793.5 eV correspond to the spin-orbit characteristics of Co³⁺, while the peak at 780.8 eV in Co 2p_{3/2} and the peak at 795.1 eV in Co 2p_{1/2} are attributed to Co²⁺ [60]. The V doping in Co₉S₈ results the Co 2p spectra shift by 0.3–0.7 eV to the higher binding energy (Fig. 2f and Fig. S12). This phenomenon ascribes to the fact that after the introduction of vanadium, Co atom in Co₉S₈ is a lost electron state relative to the original Co₉S₈. The DFT calculation on the charge density difference of V-Co₉S₈ further confirms the electron loss characteristics of cobalt after V doping

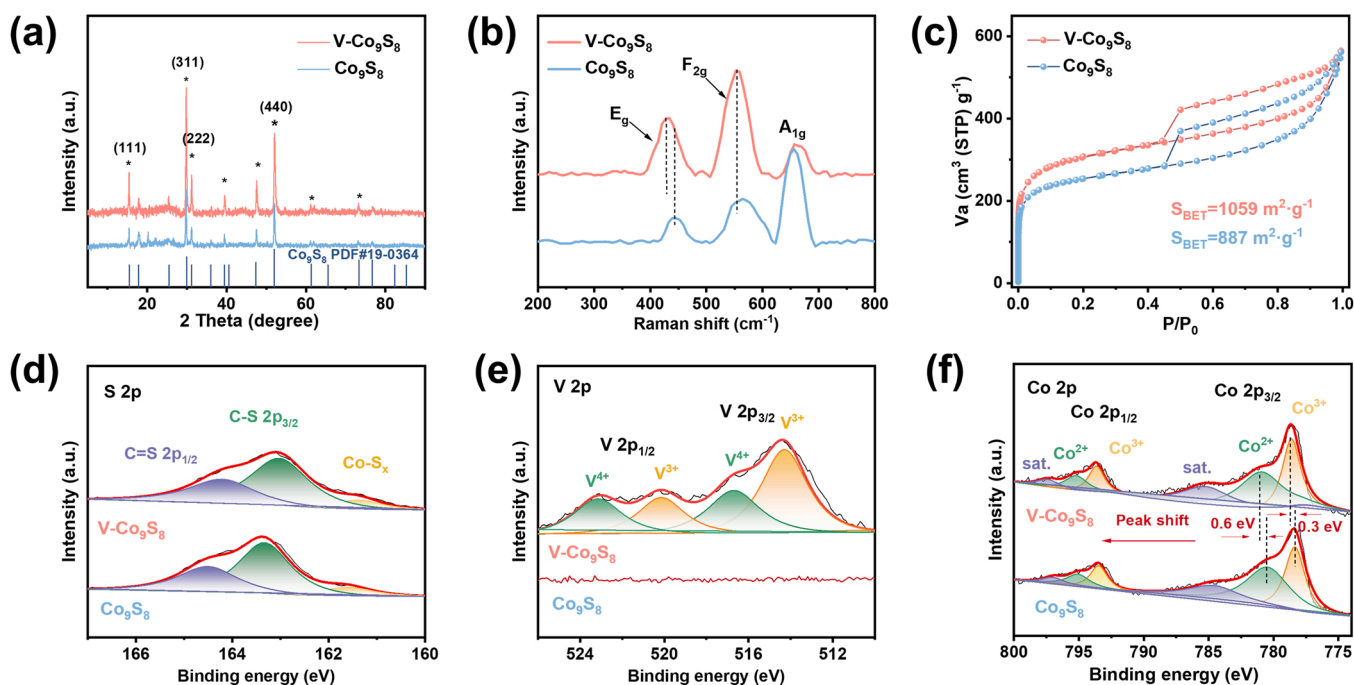


Fig. 2. (a) XRD patterns, (b) Raman spectra, (c) N₂ sorption isotherms at 77 K, and (d, e and f) high resolution S 2p, V 2p and Co 2p XPS spectra of Co₉S₈ and V-Co₉S₈.

(Fig. S13). Meanwhile, the fitted Co 2p results indicate that ratio of $\text{Co}^{3+}/\text{Co}^{2+}$ also increases from 0.47 to 0.58 with altering the vanadium doping amount, which makes Co centers in V-Co₉S₈ more positively charged and thus facilitates the electrostatic attraction of more anionic intermediates for the faster redox process in alkaline medium [61,62].

3.2. Electrocatalytic activity of V-Co₉S₈ for the ORR/OER

Cyclic voltammetry (CV) and linear sweep voltammetry (LSV) were conducted to evaluate the catalytic performance of samples toward the oxygen reaction. V-Co₉S₈ exhibits a large-area ORR peak around 0.83 V, which is an indicative of the superior oxygen reduction activity (Fig. S14a). The LSVs (Fig. 3a) show that both the onset potential (E_{onset} of 0.95 V) and the half-wave potential ($E_{1/2}$ of 0.83 V) of V-Co₉S₈ are more positive than Co₉S₈ (E_{onset} of 0.87, $E_{1/2}$ of 0.80 V). Especially, the $E_{1/2}$ of V-Co₉S₈ is close to a commercial 20 wt% Pt/C catalyst ($E_{1/2}$ of 0.84 V). The positive shift of $E_{1/2}$ of V-Co₉S₈ implies the new sites owning the higher intrinsic activity, which is expected as the vanadium modulated Co sites. For the evaluation of cost-efficiency of catalyst, the mass activity (i_m) was normalized by the total mass of the loaded Co and V. As shown in Fig. 3b, the V-Co₉S₈ shows a mass activity of 8.41 A mg⁻¹ at 0.80 V, which is as 4 times as the Co₉S₈ (2.12 A mg⁻¹) and much higher than the Pt/C (1.73 A mg⁻¹). Moreover, the transfer number of electrons (n) of V-Co₉S₈ based on the Koutecky-Levich (K-L) equation was calculated to be 4.0, which is superior to the Co₉S₈ counterpart (3.7) (Fig. S14b-d). Its high selectivity for the four-electron ORR pathway is also another evaluation criterion, as it not only determines energy conversion efficiency but also affects catalytic activity by minimizing

the poisoning species such as oxygen-containing radicals derived from the H₂O₂ by-products. The outstanding ORR kinetics of the V-Co₉S₈ is further reflected by the smallest Tafel slope of 87.5 mV dec⁻¹ comparing with the Co₉S₈ and the Pt/C (Fig. 3c). The improved activity and kinetics of V-Co₉S₈ suggest that the enhanced oxygen adsorption on the V-Co₉S₈ site as the stronger Co-O binding facilitates the subsequent O-O bond cleavage toward the direct 4-electrons ORR pathway [63].

To fulfill the requirement of bifunctional electrocatalysts for rechargeable ZABs, the OER activity of the as-prepared catalysts was also assessed. The overpotential of V-Co₉S₈ is as low as 380 mV at 10 mA cm⁻², which is 20 mV lower than the Co₉S₈ (Fig. 3d). Meanwhile, Tafel slope of V-Co₉S₈ (81.8 mV dec⁻¹) is significantly smaller than Co₉S₈ (96.9 mV dec⁻¹) and RuO₂ (187.4 mV dec⁻¹) (Fig. 3c). V-Co₉S₈ has the lowest Tafel slope and thus is the most active sample since Tafel slope reflects the OER rate mainly originating from the coverage of the adsorbed species [64]. A large number of studies show that the OER activities of Co₉S₈ is limited by the weak binding of intermediates [65, 66]. The significantly boosted OER activity is probably due to the enhanced binding affinity between the vanadium modulated Co active site and the intermediates.

The electrochemical impedance spectroscopy (EIS) was used to investigate the electrocatalytic reaction resistance and the results are shown in Fig. 3e. The V-Co₉S₈ exhibit the smaller interface charge-transfer resistance (R_{ct}) of 1.2 Ω fewer than the Co₉S₈ (1.5 Ω), indicating that the tuning electronic structure of Co₉S₈ by vanadium doping promotes the faster shuttling of electrons during OER. Furthermore, the turn over frequency (TOF) was used to further evaluate the intrinsically electrocatalytic activity of samples. TOF of the V-Co₉S₈ at 1.61 V was

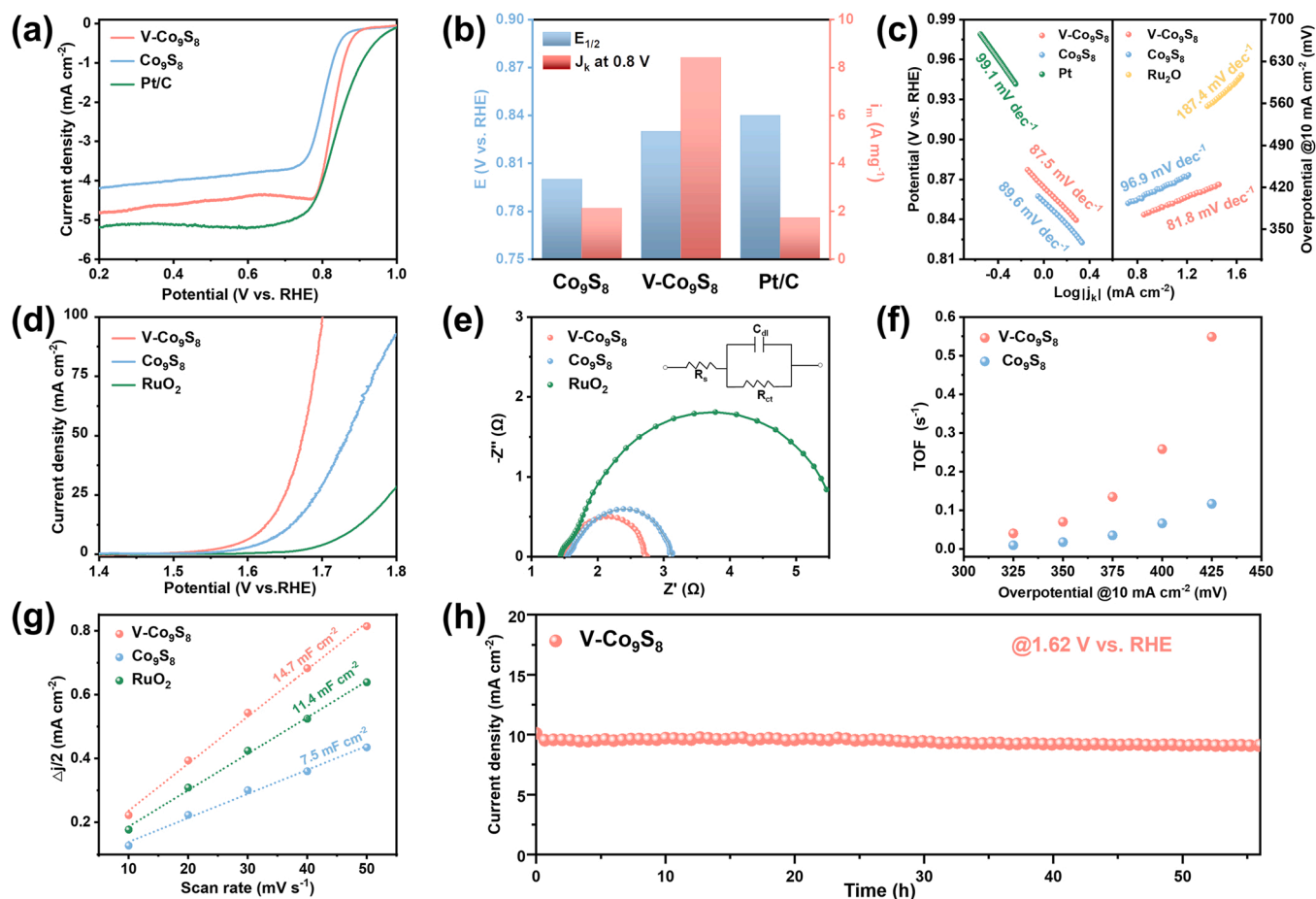


Fig. 3. Electrocatalytic performance. (a) ORR polarization curves of V-Co₉S₈, Co₉S₈ and Pt/C samples. (b) Half-wave potential ($E_{1/2}$) and mass activities (i_m) of ORR on V-Co₉S₈, Co₉S₈ and Pt/C at 0.8 V. (c) Corresponding Tafel plots of ORR and OER, (d) OER polarization curves, (e) Nyquist plots, (f) TOF values, and (g) C_{dl} of V-Co₉S₈, Co₉S₈ and RuO₂. (h) Stability test of V-Co₉S₈ at 1.62 V.

determined to be 0.14 s^{-1} , overwhelmingly exceeding that of Co_9S_8 (0.08 s^{-1}). The intrinsic activity measurements by per-site TOF (Fig. 3f) provide the evidence that V- Co_9S_8 presents the enhanced OER activity on a per-site basis since its each TOF is significantly higher than Co_9S_8 at every measured overpotential, which is consistent with the Tafel slope results (Fig. 3c). The electrochemically active surface area (ECSA) can reflect the accessibly active sites of V- Co_9S_8 and Co_9S_8 , which was estimated by measuring the electrochemical double-layer capacitance (C_{dl}) (Fig. 3g and Fig. S16). The measured C_{dl} are ~ 14.7 , 7.5 and 11.4 mF cm^{-2} for V- Co_9S_8 , Co_9S_8 and RuO_2 , respectively. The V- Co_9S_8 carbon nanoflowers can provide more accessible active area for OER and facilitate mass transfer. Simultaneously, the effects of Co and V contents in V- Co_9S_8 on the electrochemical properties were explored (Fig. S17).

However, the single-atom can be easily formed in MOF-derived materials [67,68]. In order to further verify whether the catalytic activity mainly results from atomically dispersed cobalt atoms, introduced thiocyanate ions (SCN^-) to produce toxic effects on the Co atoms. V- Co_9S_8 showed strong resistance to the SCN^- ion poisoning effect in alkaline electrolytes. The decrease in ORR performance was very limited (Fig. S18). Thus, atomically dispersed cobalt in the catalysts are not the main active sites in V- Co_9S_8 . To further study catalytic processes, we etched the inside cobalt particles in V- Co_9S_8 with the retention of possible single atoms by immersing samples in 6 M HCl solution for 3 days at 100°C (named as E-V- Co_9S_8). The ORR/OER electrochemical

activity of this treated E-V- Co_9S_8 was significantly lower than that of V- Co_9S_8 (Fig. S19). Thus, it can be confirmed that those accessible V- Co_9S_8 in the nitrogen-doped porous carbon flowers are the main sites catalyze ORR and OER. Overall, the vanadium doping on Co_9S_8 brings the enhanced intrinsic activity and the faster kinetics to make V- Co_9S_8 exhibit the better potential in using as bifunctional catalyst toward ORR and OER than the most reported Co based catalysts (Table S7 and Table S8).

3.3. Mechanism analysis

To explore the origin of the enhanced intrinsic activity and the fast kinetics of V- Co_9S_8 toward ORR, its electron-donating ability and electronic property was evaluated by the ultraviolet photoelectron spectroscopy (UPS) and the results are shown in Fig. 4a. The valence band maximum values of Co_9S_8 and V- Co_9S_8 are calculated to be 3.36 eV and 3.20 eV . The V-doping in Co_9S_8 makes the valence band shift closer to the Fermi level, which results it easier for the electrons under excitation to participate in the electrochemical reaction of oxygen reduction [69]. Since the valence electrons close to the Fermi level mainly contribute to the d orbital of transition metal [70,71], the introduction of vanadium promotes the d orbital of Co_9S_8 more close to the Fermi level, which is favorable for the adsorption of oxygen intermediates [72]. The calculated work function (ϕ is the minimum energy required to extract one

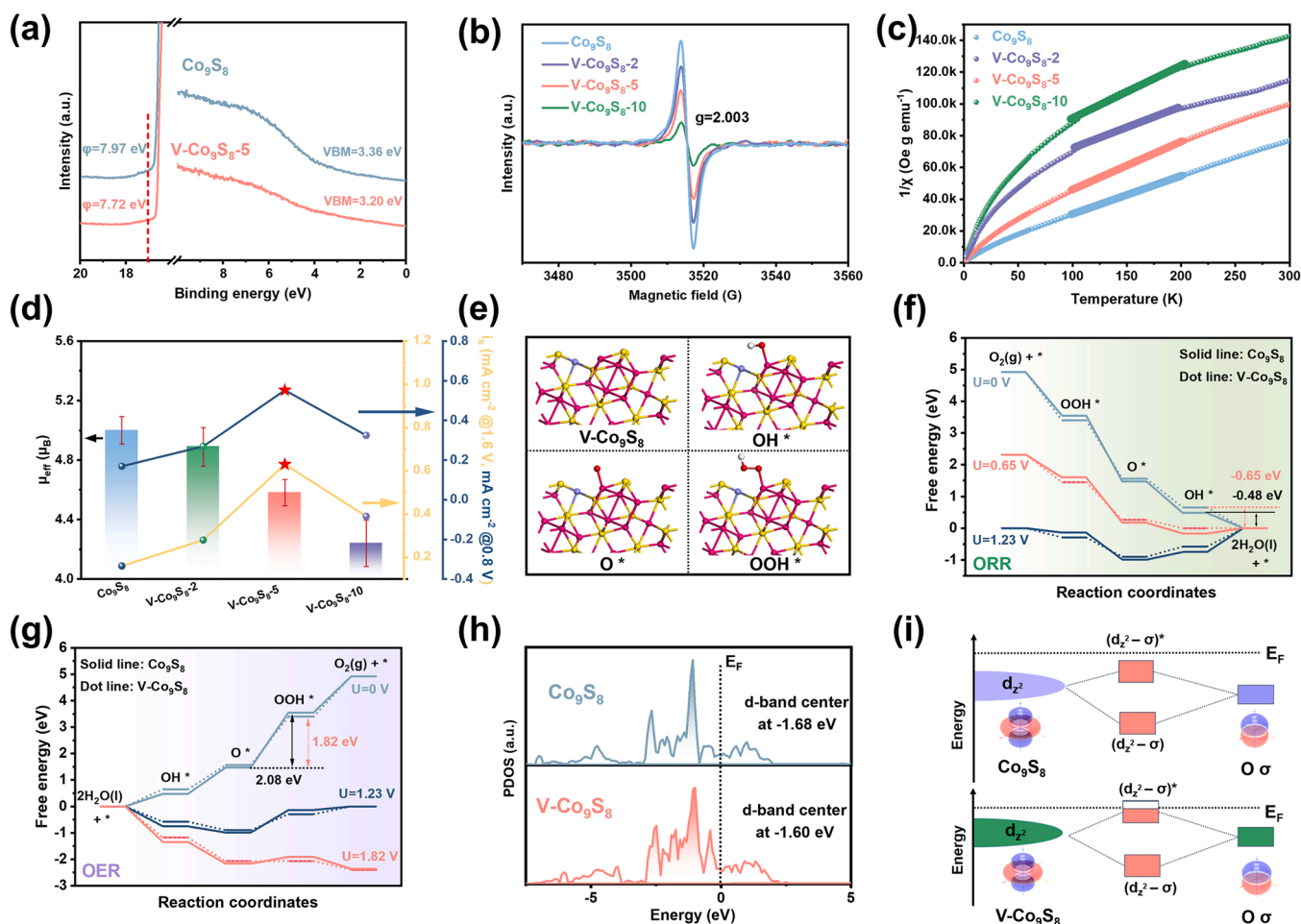


Fig. 4. (a) UPS spectra of Co_9S_8 and V- Co_9S_8 -5. (b) EPR spectra of Co_9S_8 , V- Co_9S_8 -2, V- Co_9S_8 -5, and V- Co_9S_8 -10. (c) Plots of inverse susceptibility $1/\chi$ vs temperature (the straight solid lines are the fitting results based on the Curie-Weiss law). (d) The effective magnetic moment (μ_{eff}) filling and specific activity (i_a) of Co_9S_8 , V- Co_9S_8 -2, V- Co_9S_8 -5, and V- Co_9S_8 -10. Error bars represent standard deviations. (e) The models of adsorption configuration of OER/ORR intermediate (OOH^* , O^* , and OH^*) for V- Co_9S_8 (311). (f, g) Free energy diagram of two models at different operation potentials for the ORR and OER (the double-headed arrows suggest the rate-determining steps). (h) Calculated density of states of Co_9S_8 (311) and V- Co_9S_8 (311) orbitals Co 3d and S 2p. (i) Illustration of orbital interactions between adsorbed O_2 (σ) and Co sites d_{z^2} in Co_9S_8 (311) and V- Co_9S_8 (311).

electron from the interior to the surface of a substance) values of Co_9S_8 and $\text{V-Co}_9\text{S}_8$ are 7.97 and 7.72 eV, and ϕ value decreases with the vanadium doping amount as shown in Fig. S20. The smaller ϕ of $\text{V-Co}_9\text{S}_8$ means that the V-doping lowers the energetic barrier of the catalyst donating electrons to oxygen intermediates. This kind of electron-donating ability are closely related to the spin configuration of the Co active site of $\text{V-Co}_9\text{S}_8$.

Electron paramagnetic resonance (EPR) measurements were conducted to probe the unpaired electrons on Co atom in the Co_9S_8 by regulating the vanadium doping level. As shown in Fig. 4b, the EPR spectrum of $\text{V-Co}_9\text{S}_8$ shows the lower peak intensity than Co_9S_8 , suggesting the reduced unpaired electrons in $\text{V-Co}_9\text{S}_8$, which is ascribed to the electron spin configuration transformation of partial Co atom. The electron spin configuration of Co active sites in $\text{V-Co}_9\text{S}_8$ was analyzed by the temperature-dependent magnetization (M-T) measurements. As shown in Fig. S21, the susceptibility originated from the magnetizations ($\chi = M/H$) of samples abides by a paramagnetic Curie-Weiss law: $\chi = C/(T-\Theta)$ when temperature is higher than 50 K, in which C is Curie constant and Θ is Curie-Weiss temperature. From the fitting results (Fig. 4c), an effective magnetic moment (μ_{eff}) can be calculated according to the formula of $\mu_{\text{eff}} = \sqrt{8C\mu_B}$ (Table S3). The μ_{eff} of a 3d orbital of transition metal always derives from the spin splitting of partially occupied d orbitals (e_g and t_{2g}). The vanadium doping in Co_9S_8 results in a decrease of μ_{eff} value with the doping amount, it signifies that $\text{V-Co}_9\text{S}_8$ has the lower spin state origin from the electronic redistribution where some electrons in e_g orbitals populate t_{2g} orbitals (Fig. 4d and Fig. S22).

The μ_{eff} values of $\text{V-Co}_9\text{S}_8$ are positively correlated with the intrinsic activity of $\text{V-Co}_9\text{S}_8$ (referred to as specific activity of i_s). The ORR/OER results show that the $\text{V-Co}_9\text{S}_8$ (0.55/0.63 mA cm^{-2}) with the modest doping level has highest specific activity, which brings an increase by a factor of ~ 3 as compared with Co_9S_8 (0.17/0.16 mA cm^{-2}) (Fig. 4d). This can be explained by the spatial electronic configurations of the d orbitals in the transition metals. Generally, the e_g orbital of transition metals are more readily to penetrate and overlap the antibonding σ^* -orbital of O 2p, thus influencing the bonding strength and electron-transfer rates. The moderate magnetic moment and the spin state of $\text{V-Co}_9\text{S}_8$ favor the coupling of the oxygen-containing adsorbates on metal sites and enhance the transfer of spin-oriented electrons (e_g), and thus are more conducive to the adsorption and desorption of oxygen intermediates, thereby balancing the competition of ORR/OER rate-determining steps [73,74]. Therefore, we reveal the effect of V doping in the Co_9S_8 structure on the free energy barrier of the ORR/OER rate-determining step by first-principles density functional theory (DFT) calculations. For comparison, Co_9S_8 (311) and $\text{V-Co}_9\text{S}_8$ (311) species were used as models for the calculations. The binding energies of reaction intermediates involved in ORR and OER, including O^* , OH^* and OOH^* species, were calculated for Co sites of the structural model (Fig. S23 and Table S4-5). As can be seen from the free energy pathways of the ORR process in Fig. 4f, all the electron transfer steps of $\text{V-Co}_9\text{S}_8$ electrode will carry out spontaneously at a U value of below 0.65 V, indicating all reaction steps are exothermic. The whole process is dominated by the rate-determining step: $\text{OH}^* + e^- = \text{OH}^- + *$. The results indicated higher ORR electrochemical activity of the V-doped catalyst relative to pristine Co_9S_8 . For OER, the largest potential step at the equilibrium potential (1.82 V) suggested the rate-determining step with the corresponding overpotential listed in Fig. 4g. Therefore, the V doping catalyst can effectively enhance the intrinsic activity of Co_9S_8 catalyst by reducing the free energy at ORR/OER rate-determining steps, which is in agreement with the electrochemical results.

To confirm how V-doping optimize the orbital electronic occupation of Co_9S_8 , the DFT computations were performed using Vienna ab initio simulation package (VASP). Fig. S24 displays the Co_9S_8 (311) plane and $\text{V-Co}_9\text{S}_8$ (311) crystal plane. The Co 3d and S 2p centers for Co_9S_8 and $\text{V-Co}_9\text{S}_8$ were determined by integrating the projected density of states (PDOS), as illustrated in Fig. S25. The results manifest the metallic

character with zero band gaps, indicating the easy transfer of electrons in samples. As demonstrated in Fig. 4h, the d -band center increases from -1.68 eV in the Co_9S_8 to -1.60 eV in the $\text{V-Co}_9\text{S}_8$, it leads to an increase the binding strength of oxygen intermediates. Moreover, the energy difference between the Co 3d and the S 2p centers (Fig. S26 and Table S6) is smaller in $\text{V-Co}_9\text{S}_8$ than in Co_9S_8 , suggesting a decrease in the number of the unpaired electrons and an enhancement of Co-S covalency. The results of DFT are consistent with the effective magnetic moment to prove that the vanadium doping in Co_9S_8 can facilitate the electron exchange between the Co sites and the adsorbed oxygen intermediates to accelerate the oxygen redox rates [75-77].

The contribution of the five 3d orbitals to the density of states of Co in the $\text{V-Co}_9\text{S}_8$ was further analyzed. The d_{z^2} orbital in the e_g orbital of Co overlaps with the p-orbitals of oxygen intermediates, which determines the ORR/OER activity. As shown in Fig. S27 and S28, the d_{z^2} -orbital density around the Fermi level of Co atom has a significant increase after the V doping. As shown in Fig. 4i, the orbital hybridization between Co d_{z^2} and O_2 σ is analyzed. The Co d_{z^2} orbital of $\text{V-Co}_9\text{S}_8$ possesses the higher energy level than the Co_9S_8 , in which the unpaired d_{z^2} electron of Co can be readily injected into the antibonding σ -orbital of oxygen. The interactions of Co d_{z^2} - O_2 σ are strong enough to split into the bonding orbitals (d_{z^2} - σ) and the antibonding orbitals (d_{z^2} - σ^*). Compared with the Co_9S_8 , the (d_{z^2} - σ^*) of $\text{V-Co}_9\text{S}_8$ exhibits the higher energy level and the lower electron occupancy, which is more prone to the oxygen adsorption and to enhance the interaction of Co- O_2 . The adsorption energy of O_2 on the $\text{V-Co}_9\text{S}_8$ and the Co_9S_8 is estimated as a descriptor for ORR/OER activity.

As the newly developed $\text{V-Co}_9\text{S}_8$ catalyst has highly intrinsic bifunctional catalytic performance for ORR and OER, we further evaluated its long-term stability test to confirm the catalyst's potential for practical application. It is generally believed that the transition metal encapsulated in graphene shells have been considered relatively stable and does not change during the catalytic process [78]. To check the possible change of catalysts in the electrochemical reduction and oxidation after long-cycle testing (denote as: post-ORR and post-OER, respectively). The detailed results are shown in Fig. S29 and S30, which revealed that the post-ORR $\text{V-Co}_9\text{S}_8$ showed similar properties to the as-prepared $\text{V-Co}_9\text{S}_8$, including the morphology (Fig. S29), phase, component and surface electronic states (Fig. S30a-d), suggesting that the $\text{V-Co}_9\text{S}_8$ was stable with no significant change during the catalytic ORR process. For the post-OER $\text{V-Co}_9\text{S}_8$, the nanoflower structure of $\text{V-Co}_9\text{S}_8$ is maintained while the XRD pattern revealed that crystallinity degree of the post-OER $\text{V-Co}_9\text{S}_8$ decreased greatly (Fig. S30a). The XPS results revealed a significant increase in the oxygen content and decrease in the carbon content compared with the as-prepared $\text{V-Co}_9\text{S}_8$ (Fig. S30b). Furthermore, the O 1s spectrum of XPS shows a main peak of 531.2 eV and two small peaks of 529.9 eV and 533.5 eV, corresponding to C=O bond, Co-O bond and surface adsorbed hydroxyl group, respectively, which reveals the formation of the CoOOH layer (Fig. S30c) [79]. Consequently, the binding energy of the Co species in the post-OER $\text{V-Co}_9\text{S}_8$ is positively shifted to the oxidation state and exists in the oxidation state ($\text{Co}^{2+}/\text{Co}^{3+}$) and the conversion process of Co species can be confirmed by CV curves (Fig. S31). Surprisingly, TEM and HR-TEM images show that the post-OER $\text{V-Co}_9\text{S}_8$ exhibits an interface between amorphous CoOOH and crystalline Co_9S_8 in the high-voltage long-term stability test at 1.61 V (Fig. 3h and Fig. S32). As recently suggested by many researchers, the in-situ conversion of the pristine electrocatalyst during OER is critical for their high performance, and the intermediates are identified as the real active sites [79]. Taking Co-based electrocatalysts as an example, recent operando evidence suggests the conversion of Co^{2+} ($\text{Co}(\text{OH})_2$, CoO_x) to Co^{3+} (CoOOH) as a pre-catalytic electrochemical process, and both oxidized forms of Co^{2+} and Co^{3+} , are assigned for OER activity [80,81]. In such cases, the pristine electrocatalysts are the pre-catalyst for active site production. A similar phenomenon thus occurs for $\text{V-Co}_9\text{S}_8$, as the mechanism of OER requires the formation of M-OH and electrooxidation to M-OOH

(M=metal) [82,83], which implies replacement of the coordination-linked molecule with hydroxide ions. Therefore, the CoOOH/Co₉S₈ and CoOOH/V-Co₉S₈ heterostructures were formed as the real active sites of OER, and the essential reasons for the difference in the formation activities of the heterostructures were explored combined with theoretical calculations analyses (Fig. S33). The formation energy of CoOOH/V-Co₉S₈ heterostructure reasonably exhibited through tailored the conduction band minimum (CBM) level of the Co₉S₈ species by vanadium doping. Therefore, promoted electron interaction can be generated through lowering the CBM level of Co-S to tailor the energy barrier required for the electron transfer from the VBM of CoOOH to the CBM of Co-S, thereby accelerating the rate-determining step of the oxygen evolution reaction. As shown in Fig. S33a-b, V-Co₉S₈ displays the smallest energy gap (E_g) value than Co₉S₈, suggesting the most favorable electron transfer rate. Fig. S33c shows the CBM levels of Co₉S₈ are higher than the VBM level of CoOOH, suggesting additional energy is required to achieve the electron transfer from the VBM of CoOOH to the CBM of Co₉S₈. It should be noted that V-Co₉S₈ possesses the lowest CBM level than Co₉S₈, which is closest to the VBM of CoOOH, indicating that CoOOH is more likely to interact with reactive species on the surface of V-Co₉S₈. The total density of states and band structures of CoOOH/V-Co₉S₈ (Fig. S33d-f) shows that CoOOH/V-Co₉S₈ possess the lowest band gap, suggesting the lowest conversion energy for the formation of Co³⁺ species and best conductivity of CoOOH/V-Co₉S₈. [84,85].

3.4. As bifunctional catalyst for the air cathode of ZABs

Since the experimental and theoretical studies have well demonstrated that V-Co₉S₈ owns the intrinsic and enhanced activity on both the ORR and the OER, it is strongly encouraged to apply the V-Co₉S₈ as a bifunctional catalyst in metal-air batteries. Herein, the rechargeable ZABs were assembled as schematically shown in Fig. 5a to study the performance of V-Co₉S₈ as the catalyst of air cathode. As shown in Fig. 5b, the V-Co₉S₈ based ZAB shows the higher voltage window of ≈ 1.43 V than the battery with the catalysts of Co₉S₈ (≈ 1.38 V) or the Pt/C+RuO₂ (≈ 1.41 V), confirming the better ability of V-Co₉S₈ to drive the air cathode of ZABs. Meanwhile, Fig. S34 practically illustrates the capability that the V-Co₉S₈ based ZABs power 3.0 V light-emitting diode devices. Moreover, the V-Co₉S₈ based ZAB exhibits a power density of 300 mW cm^{-2} at 0.6 V , while gives the peak power density of 345 mW cm^{-2} (Fig. 5c and S35). The charge-discharge polarization curves (Fig. S36) show a much higher current density and the shallower voltage gap of V-Co₉S₈ based ZAB than the other two catalysts driving ZABs, revealing that V-Co₉S₈ renders the air cathode of ZAB an enhanced catalytic activity and an improved energy efficiency. In the galvanostatic full-discharge tests (Fig. 5d), V-Co₉S₈ based ZAB displays the higher voltage plateau than the ZABs with Co₉S₈ or Pt/C+RuO₂, confirming the superior ORR activity of V-Co₉S₈. Especially fascinating, the specific capacity of V-Co₉S₈ based ZABs reaches $814.3 \text{ mAh g}_{\text{Zn}}^{-1}$ at

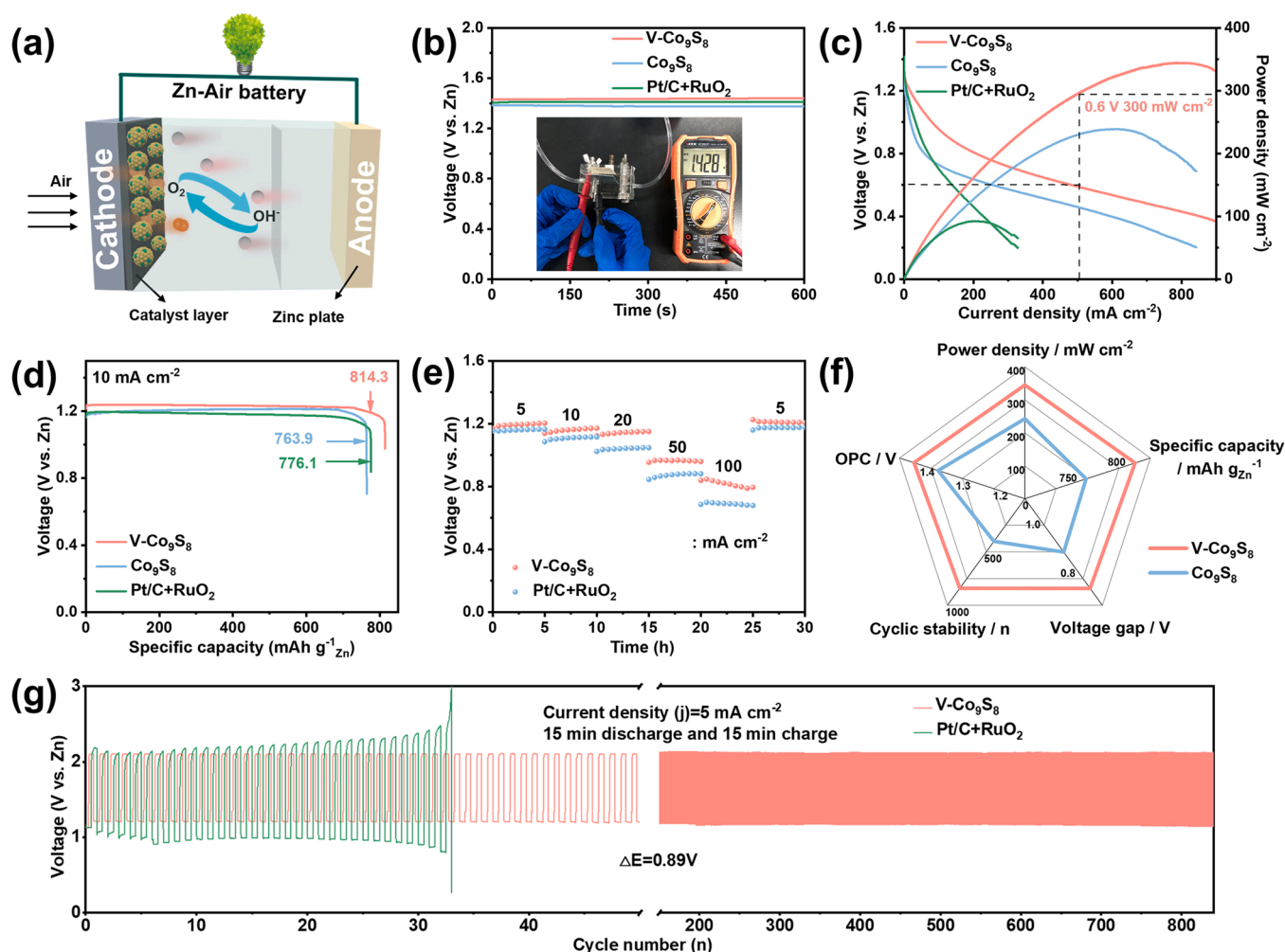


Fig. 5. (a) Schematic depictions of the rechargeable ZABs device. (b) Open-circuit voltages, (c) discharge and power density curves of V-Co₉S₈, Co₉S₈ and Pt/C+RuO₂ as the air electrode catalyst. (d) Voltage vs. specific capacity curves at a constant current density of 10 mA cm^{-2} . (e) Discharge curves of V-Co₉S₈ and Pt/C+RuO₂ with current densities from 5 to 100 mA cm^{-2} . (f) A radar plot comparison of OPC, power density, specific capacity, voltage gap and cyclic stability for Co₉S₈ and V-Co₉S₈. (g) Cycling performance of V-Co₉S₈ and the commercial Pt/C+RuO₂ (5 mA cm^{-2}).

10 mA cm⁻², which is superior to the ZABs with the Co₉S₈ (763.9 mAh g_{Zn}⁻¹) or the Pt/C+RuO₂ (776.6 mAh g_{Zn}⁻¹). Meanwhile, the signifying energy density of V-Co₉S₈ based ZAB (1001 Wh kg⁻¹) is close to the theoretical energy density of metal zinc (1086 Wh kg⁻¹).

Rate capability and durability are also crucial to the practical applications of ZABs. Galvanostatic discharge tests were carried out to assess the rate performance of the V-Co₉S₈ based ZABs (Fig. 5e) [86]. The V-Co₉S₈ cathode successfully renders the ZABs the higher output voltages, i.e., 1.20, 1.00 and 0.85 V at 5, 50 and 100 mA cm⁻² than the Pt/C+RuO₂ cathode of 1.18, 0.90 and 0.72 V at the corresponding current density. Reversely, the current returns to 5 mA cm⁻² when the voltage recovers to 1.20 V, implying the superb rate stability of V-Co₉S₈ cathode. The radar plot in Fig. 5f well illustrates the much better properties of V-Co₉S₈ with respect to power density, specific capacity and cyclic stability than the Co₉S₈. For the practical application, the remarkably cycling stability of the ZABs with V-Co₉S₈ is exhibited by Fig. 5g and Fig. S37. The ZAB can operate more than 840 cycles (over 420 h, i.e., >17 days) at 5 mA cm⁻², and the voltage gap slightly increases by 0.06 V. Even at the higher current density of 10 mA cm⁻², the V-Co₉S₈ cathode also affords extraordinary durability with the lifespan of 1200 cycles and the low voltage gap of 1.10 V.

Comparing with the recently reported state-of-the-art Co based catalysts, besides the superior energy density and power density, V-Co₉S₈ based ZAB exhibits the extraordinary durability (Table S9). The significant advances could be attributed to that the vanadium doping in Co₉S₈ modulates electronic structure to enhance the intrinsic activity of V-Co₉S₈, which lower the energy barrier for the adsorption of oxygen intermediates and reinforce the interaction between the catalysts and the oxygen intermediates. The nitrogen-doped carbon NFs anchored with V-Co₉S₈ facilitate the quick mass transport and prevent catalysts nanoparticles from agglomeration and immigration.

4. Conclusions

The tunable vanadium-doped Co₉S₈ (V-Co₉S₈) nanoparticles encapsulated in nitrogen-doped porous carbon nanoflowers (NFs) have been successfully prepared by an innovative double-solvent approach (DSA). The magnetic measurements and the theoretical calculations demonstrate that the spin state of Co can be optimized through a modest V-doping level in V-Co₉S₈. The modestly modulated electronic structure of V-Co₉S₈ enables the enhanced Co-S covalency, which balances the adsorption/desorption of oxygen intermediates and exhibits a superior bifunctional activity on both the ORR and the OER. The assembled ZAB using V-Co₉S₈ as catalyst of air cathode supplies a power density of 345 mW cm⁻², an energy density of 814 mAh g_{Zn}⁻¹ and an extraordinary cycling-stability of > 840 cycles at 5 mA cm⁻². The performance of V-Co₉S₈ based ZABs outperforms the noble catalysts (Pt/C and RuO₂) and most Co based catalysts reported recently. The present work could provide a valuable guidance for the engineering in electronic spin state of catalysts to develop the electrochemical energy storage and conversion systems.

CRediT authorship contribution statement

Lin Wu: Investigation, Conceptualization, Data curation, Methodology, Project administration, Formal analysis, Writing – original draft. **Shuxin Li:** Conceptualization, Methodology, Physicochemical characterization. **Lixiang Li:** Project administration, Writing – review & editing, Formal analysis. **Han Zhang:** Project administration, Data curation, Writing – review & editing. **Li Tao:** Data curation, Formal analysis. **Xin Geng:** Methodology, Formal analysis. **Haiming Yang:** Formal analysis. **Weimin Zhou:** Formal analysis. **Chengguo Sun:** Formal analysis. **Dongying Ju:** Methodology, Formal analysis. **Baigang An:** Supervision, Project administration, Methodology, Writing – review & editing.

Declaration of Competing Interest

The authors declare that they have no known competing financial interests or personal relationships that could have appeared to influence the work reported in this paper.

Data Availability

Data will be made available on request.

Acknowledgements

The financial supports from National Natural Science Foundation of China (NSFC, No. 51872131, 51972156, 51672117, 51672118, 21701077 and 22109061), University of Science and Technology Liaoning Talent Project Grants (601010326), Talent Project of Revitalizing LiaoNing (2020LNQN17, 2019QN07) and the Distinguished Professor Project of Education Department of Liaoning are acknowledged.

Appendix A. Supporting information

Supplementary data associated with this article can be found in the online version at doi:10.1016/j.apcatb.2022.122250.

References

- [1] X. Wan, X. Liu, Y. Li, R. Yu, L. Zheng, W. Yan, H. Wang, M. Xu, J. Shui, Fe-N-C electrocatalyst with dense active sites and efficient mass transport for high-performance proton exchange membrane fuel cells, *Nat. Catal.* 2 (2019) 259–268.
- [2] N.V. Boas, J.B.S. Junior, L.C. Varanda, S.A.S. Machado, M.L. Calegari, Bismuth and cerium doped cryptomelane-type manganese dioxide nanorods as bifunctional catalysts for rechargeable alkaline metal-air batteries, *Appl. Catal. B: Environ.* 258 (2019), 118014.
- [3] Y.J. Li, L. Cui, P.F. Da, K.W. Qiu, W.J. Qin, W.B. Hu, X.W. Du, K. Davey, T. Ling, S. Z. Qiao, Multiscale structural engineering of Ni-Doped CoO nanosheets for zinc-air batteries with high power density, *Adv. Mater.* 30 (2018) 1804653.
- [4] S. Ramakrishnan, D.B. Velusamy, S. Sengodan, G. Nagaraju, D.H. Kim, A.R. Kim, D. J. Yoo, Rational design of multifunctional electrocatalyst: An approach towards efficient overall water splitting and rechargeable flexible solid-state zinc-air battery, *Appl. Catal. B: Environ.* 300 (2022), 120752.
- [5] H. Ge, G. Li, J. Shen, W. Ma, X. Meng, L. Xu, Co₄N nanoparticles encapsulated in N-doped carbon box as tri-functional catalyst for Zn-air battery and overall water splitting, *Appl. Catal. B: Environ.* 275 (2020), 119104.
- [6] Y.P. Deng, Y. Jiang, R. Liang, S.J. Zhang, D. Luo, Y. Hu, X. Wang, J.T. Li, A. Yu, Z. Chen, Dynamic electrocatalyst with current-driven oxyhydroxide shell for rechargeable zinc-air battery, *Nat. Commun.* 11 (2020) 1–10.
- [7] H. Jiang, J. Xia, L. Jiao, X. Meng, P. Wang, C.S. Lee, W. Zhang, Ni single atoms anchored on N-doped carbon nanosheets as bifunctional electrocatalysts for Urea-assisted rechargeable Zn-air batteries, *Appl. Catal. B: Environ.* 310 (2022), 121352.
- [8] S. Li, H. Zhang, L. Wu, H. Zhao, L. Li, C. Sun, B. An, Vacancy-engineered CeO₂/Co heterostructure anchored on the nitrogen-doped porous carbon nanosheet arrays vertically grown on carbon cloth as an integrated cathode for the oxygen reduction reaction of rechargeable Zn-air battery, *J. Mater. Chem. A* 10 (2022) 9858–9868.
- [9] Y. Meng, J.C. Li, S.Y. Zhao, C. Shi, X.Q. Li, L. Zhang, P.X. Hou, C. Liu, H.M. Cheng, Fluorination-assisted preparation of self-supporting single-atom Fe-N-doped single-wall carbon nanotube film as bifunctional oxygen electrode for rechargeable Zn-Air batteries, *Appl. Catal. B: Environ.* 294 (2021), 120239.
- [10] X. Shu, M. Yang, D. Tan, K. San Hui, K.N. Hui, J. Zhang, Recent advances in the field of carbon-based cathode electrocatalysts for Zn-air batteries, *Mater. Adv.* 2 (2021) 96–114.
- [11] Z. Zhao, C. Chen, Z. Liu, J. Huang, M. Wu, H. Liu, Y. Li, Y. Huang, Pt-based nanocrystal for electrocatalytic oxygen reduction, *Adv. Mater.* 31 (2019) 1808115.
- [12] X. Lu, C. Zhao, Electrodeposition of hierarchically structured three-dimensional nickel-iron electrodes for efficient oxygen evolution at high current densities, *Nat. Commun.* 6 (2015) 1–7.
- [13] C. Zhang, G. Zhang, H. Li, Y. Chang, Z. Chang, J. Liu, X. Sun, Interfacial dehalogenation-enabled hollow N-doped carbon network as bifunctional catalysts for rechargeable Zn-air battery, *Electrochim. Acta* 247 (2017) 1044–1051.
- [14] F. Cheng, J. Shen, B. Peng, Y. Pan, Z. Tao, J. Chen, Rapid room-temperature synthesis of nanocrystalline spinels as oxygen reduction and evolution electrocatalysts, *Nat. Chem.* 3 (2011) 79–84.
- [15] J. Zhang, J. Chen, Y. Luo, Y. Chen, C. Zhang, Y. Luo, Y. Xue, H. Liu, G. Wang, R. Wang, Engineering heterointerfaces coupled with oxygen vacancies in lanthanum-based hollow microspheres for synergistically enhanced oxygen electrocatalysis, *J. Energy Chem.* 60 (2021) 503–511.
- [16] C. Wei, Z. Feng, G.G. Scherer, J. Barber, Y. Shao-Horn, Z. Xu, Cations in octahedral sites: a descriptor for oxygen electrocatalysis on transition-metal spinels, *Adv. Mater.* 29 (2017) 1606800.

- [17] S. Deng, Y. Zhong, Y. Zeng, Y. Wang, X. Wang, X. Lu, X. Xia, J. Tu, Hollow TiO₂@Co₉S₈ core-branch arrays as bifunctional electrocatalysts for efficient oxygen/hydrogen production, *Adv. Sci.* 5 (2018) 1700772.
- [18] X. Li, Z. Kou, S. Xi, W. Zhang, T. Yang, L. Zhang, J. Wang, Porous NiCo₂S₄/FeOOH nanowire arrays with rich sulfide/hydroxide interfaces enable high OER activity, *Nano Energy* 78 (2020), 105230.
- [19] A. Parra-Puerto, K.L. Ng, K. Fahy, A.E. Goode, M.P. Ryan, A. Kucernak, Supported transition metal phosphides: activity survey for HER, ORR, OER, and corrosion resistance in acid and alkaline electrolytes, *ACS Catal.* 9 (2019) 11515–11529.
- [20] M. Wu, G. Zhang, J. Qiao, N. Chen, W. Chen, S. Sun, Ultra-long life rechargeable zinc-air battery based on high-performance trimetallic nitride and NCNT hybrid bifunctional electrocatalysts, *Nano Energy* 61 (2019) 86–95.
- [21] X. Xu, S. Wang, S. Guo, K. San Hui, J. Ma, D.A. Dinh, K.N. Hui, H. Wang, L. Zhang, G. Zhou, Cobalt phosphosulfide nanoparticles encapsulated into heteroatom-doped carbon as bifunctional electrocatalyst for Zn-air battery, *Adv. Powder Mater.* 1 (2022), 100027.
- [22] J. Bai, T. Meng, D. Guo, S. Wang, B. Mao, M. Cao, Co₉S₈@MoS₂ core-shell heterostructures as trifunctional electrocatalysts for overall water splitting and Zn-air batteries, *ACS Appl. Mater. Interfaces* 10 (2018) 1678–1689.
- [23] Y. Li, R. Cao, L. Li, X. Tang, T. Chu, B. Huang, K. Yuan, Y. Chen, Simultaneously integrating single atomic cobalt sites and Co₉S₈ nanoparticles into hollow carbon nanotubes as trifunctional electrocatalysts for Zn-air batteries to drive water splitting, *Small* 16 (2020) 1906735.
- [24] K. Tang, C. Yuan, Y. Xiong, H. Hu, M. Wu, Inverse-opal-structured hybrids of N, S-codoped-carbon-confined Co₉S₈ nanoparticles as bifunctional oxygen electrocatalyst for on-chip all-solid-state rechargeable Zn-air batteries, *Appl. Catal. B: Environ.* 260 (2020), 118209.
- [25] D. Lyu, S. Yao, A. Ali, Z.Q. Tian, P. Tsiakaras, P. Shen, N. S codoped carbon matrix-encapsulated Co₉S₈ nanoparticles as a highly efficient and durable bifunctional oxygen redox electrocatalyst for rechargeable Zn-air batteries, *Adv. Energy Mater.* 11 (2021) 2101249.
- [26] W. Li, Y. Li, H. Fu, G. Yang, Q. Zhang, S. Chen, F. Peng, Phosphorus doped Co₉S₈@CS as an excellent air-electrode catalyst for zinc-air batteries, *Chem. Eng. J.* 381 (2020), 122683.
- [27] Y. Zhang, N. Wang, P. Xue, Y. Liu, B. Tang, Z. Bai, S. Dou, Co₉S₈@carbon nanospheres as high-performance anodes for sodium ion battery, *Chem. Eng. J.* 343 (2018) 512–519.
- [28] K. Tang, C. Yuan, Y. Xiong, H. Hu, M. Wu, Inverse-opal-structured hybrids of N, S-codoped-carbon-confined Co₉S₈ nanoparticles as bifunctional oxygen electrocatalyst for on-chip all-solid-state rechargeable Zn-air batteries, *Appl. Catal. B: Environ.* 260 (2020), 118209.
- [29] Q. Liu, X. Hong, X. Zhang, W. Wang, W. Guo, X. Liu, M. Ye, Hierarchically structured Co₉S₈@NiCo₂O₄ nanobrushes for high-performance flexible asymmetric supercapacitors, *Chem. Eng. J.* 356 (2019) 985–993.
- [30] X. Li, K. Li, S. Zhu, K. Fan, L. Lyu, H. Yao, Y. Li, J. Hu, H. Huang, Y. Mai, Fiber-in-Tube Design of Co₉S₈-Carbon/Co₉S₈: Enabling Efficient Sodium Storage, *Angew. Chem. Int. Ed.* 131 (2019) 6305–6309.
- [31] M. Mavrikakis, B. Hammer, J.K. Nørskov, Effect of strain on the reactivity of metal surfaces, *Phys. Rev. Lett.* 81 (1998) 2819.
- [32] H. Xin, A. Vojvodic, J. Voss, J.K. Nørskov, Abild-Pedersen, Effects of d-band shape on the surface reactivity of transition-metal alloys, *Phys. Rev. B* 89 (2014), 115114.
- [33] T. Bligaard, J.K. Nørskov, Ligand effects in heterogeneous catalysis and electrochemistry, *Electrochim. Acta* 52 (2007) 5512–5516.
- [34] Y. Ying, K. Fan, X. Luo, J. Qiao, H. Huang, Unravelling the origin of bifunctional OER/ORR activity for single-atom catalysts supported on C₂N by DFT and machine learning, *J. Mater. Chem. A* 9 (2021) 16860–16867.
- [35] Y. Rao, S. Chen, Q. Yue, Y. Kang, Optimizing the spin states of mesoporous Co₃O₄ nanorods through vanadium doping for long-lasting and flexible rechargeable Zn-air batteries, *ACS Catal.* 11 (2021) 8097–8103.
- [36] J. Qian, T. Wang, Z. Zhang, Y. Liu, J. Gao, Engineered spin state in Ce doped LaCoO₃ with enhanced electrocatalytic activity for rechargeable Zn-Air batteries, *Nano Energy* 74 (2020), 104948.
- [37] Z. Chen, Y. Song, J. Cai, X. Zheng, D. Han, Y. Wu, Y. Zang, S. Niu, Y. Liu, J. Zhu, Tailoring the d-band centers enables Co₄N nanosheets to be highly active for hydrogen evolution catalysis, *Angew. Chem.* 130 (2018) 5170–5174.
- [38] S. Huang, H. Zhang, J. Zhuang, M. Zhou, M. Gao, F. Zhang, Q. Wang, Redox-mediated two-electron oxygen reduction reaction with ultrafast kinetics for Zn-air flow battery, *Adv. Energy Mater.* 12 (2022) 2103622.
- [39] Y. Dai, J. Yu, J. Wang, Z. Shao, D. Guan, Y.C. Huang, M. Ni, Bridging the charge accumulation and high reaction order for high-rate oxygen evolution and long stable Zn-air batteries, *Adv. Funct. Mater.* 32 (2022) 2111989.
- [40] C.C. Weng, J.T. Ren, H.Y. Wang, X.W. Lv, Y.J. Song, Y.S. Wang, L. Chen, W. Tian, Z.Y. Yuan, Triple-phase oxygen electrocatalysis of hollow spherical structures for rechargeable Zn-Air batteries, *Appl. Catal. B: Environ.* 307 (2022), 121190.
- [41] H. Jiang, J. Xia, L. Jiao, X. Meng, P. Wang, C.S. Lee, W. Zhang, Ni single atoms anchored on N-doped carbon nanosheets as bifunctional electrocatalysts for Urea-assisted rechargeable Zn-air batteries, *Appl. Catal. B: Environ.* 310 (2022), 121352.
- [42] P. Serra-Crespo, E.V. Ramos-Fernandez, J. Gascon, F. Kapteijn, Synthesis and characterization of an amino functionalized MIL-101 (Al): separation and catalytic properties, *Chem. Mater.* 23 (2011) 2565–2572.
- [43] B.Y. Xia, Y. Yan, N. Li, H.B. Wu, X. Lou, X. Wang, A metal-organic framework-derived bifunctional oxygen electrocatalyst, *Nat. Energy* 1 (2016) 1–8.
- [44] W. Kohn, L. Sham, Self-consistent equations including exchange and correlation effects, 140 (1965) A1133.
- [45] S.J. Grimme, Semiempirical GGA-type density functional constructed with a long-range dispersion correction, *J. Comput. Chem.* 27 (2006) 1787–1799.
- [46] J.K. Nørskov, J. Rossmeisl, A. Logadottir, L. Lindqvist, J.R. Kitchin, T. Bligaard, H. Jónsson, Origin of the overpotential for oxygen reduction at a fuel-cell cathode, *J. Phys. Chem. B* 108 (2004) 17886–17892.
- [47] H. Zhang, Z. Zhao, Y.N. Hou, Y. Tang, Y. Dong, S. Wang, X. Hu, Z. Zhang, X. Wang, J. Qiu, Nanopore-confined g-C₃N₄ nanodots in N, S co-doped hollow porous carbon with boosted capacity for lithium-sulfur batteries, *J. Mater. Chem. A* 6 (2018) 7133–7141.
- [48] A. Aijaz, A. Karkamkar, Y.J. Choi, N. Tsumori, E. Rönnebro, T. Autrey, H. Shioyama, Q. Xu, Immobilizing highly catalytically active Pt nanoparticles inside the pores of metal-organic framework: a double solvents approach, *J. Am. Chem. Soc.* 134 (2012) 13926–13929.
- [49] W. Xia, R. Zou, L. An, D. Xia, S. Guo, E. Science, A metal-organic framework route to in situ encapsulation of Co@Co₃O₄@C core@birell nanoparticles into a highly ordered porous carbon matrix for oxygen reduction, *Energy Environ. Sci.* 8 (2015) 568–576.
- [50] B. Dong, J.Y. Xie, N. Wang, W.K. Gao, Y. Ma, T.S. Chen, X.T. Yan, Q.Z. Li, Y. L. Zhou, Y.M. Chai, Zinc ion induced three-dimensional Co₉S₈ nano-neuron network for efficient hydrogen evolution, *Renew. Energy* 157 (2020) 415–423.
- [51] T. Zhou, H. Shan, H. Yu, C. Zhong, J. Ge, N. Zhang, W. Chu, W. Yan, Q. Xu, H. Wu, Nanopore confinement of electrocatalysts optimizing triple transport for an ultrahigh-power-density zinc-air fuel cell with robust stability, *Adv. Mater.* 32 (2020) 2003251.
- [52] Y. Wang, Z. Meng, X. Gong, C. Jiang, C. Zhang, J. Xu, Y. Li, J. Bao, Y. Cui, H. Wang, Enhancing stability of Co₉S₈ by iron incorporation for oxygen evolution reaction and supercapacitor electrodes, *Chem. Eng. J.* 431 (2021), 133980.
- [53] R.M. Ouyang, Exploiting ionic radii for rational design of halide perovskites, *Chem. Mater.* 32 (2019) 595–604.
- [54] Y. Rao, S. Chen, Q. Yue, Y. Kang, Optimizing the spin states of mesoporous Co₃O₄ nanorods through vanadium doping for long-lasting and flexible rechargeable Zn-air batteries, *ACS Catal.* 11 (2021) 8097–8103.
- [55] P. Zeng, J. Li, M. Ye, K. Zhuo, Z. Fang, In situ formation of Co₉S₈/N-C hollow nanospheres by pyrolysis and sulfurization of ZIF-67 for high-performance lithium-ion batteries, *Chem. Eur. J.* 23 (2017) 9517–9524.
- [56] N. Kornienko, J. Resasco, N. Becknell, C.M. Jiang, Y.S. Liu, K. Nie, X. Sun, J. Guo, S. R. Leone, P. Yang, Operando spectroscopic analysis of an amorphous cobalt sulfide hydrogen evolution electrocatalyst, *J. Am. Chem. Soc.* 137 (2015) 7448–7455.
- [57] C. Zhao, C. Yu, M. Zhang, Q. Sun, S. Li, M.N. Banis, X. Han, Q. Dong, J. Yang, G. Wang, Enhanced sodium storage capability enabled by super wide-interlayer-spacing MoS₂ integrated on carbon fibers, *Nano Energy* 41 (2017) 66–74.
- [58] R. Ryoo, I.S. Park, S. Jun, C.W. Lee, M. Kruk, M. Jaroniec, Synthesis of ordered and disordered silicas with uniform pores on the border between micropore and mesopore regions using short double-chain surfactants, *J. Am. Chem. Soc.* 123 (2001) 1650–1657.
- [59] C. Sun, J. Ding, H. Wang, J. Liu, X. Han, Y. Deng, C. Zhong, W. Hu, Cobalt sulfides constructed heterogeneous interfaces decorated on N, S-codoped carbon nanosheets as a highly efficient bifunctional oxygen electrocatalyst, *J. Mater. Chem. A* 9 (2021) 13926–13935.
- [60] C. Sun, J. Ding, H. Wang, J. Liu, X. Han, Y. Deng, C. Zhong, W. Hu, Cobalt sulfides constructed heterogeneous interfaces decorated on N,S-codoped carbon nanosheets as a highly efficient bifunctional oxygen electrocatalyst, *J. Mater. Chem. A* 9 (2021) 13926–13935.
- [61] K. Liu, J. Li, Q. Wang, X. Wang, D. Qian, J. Jiang, J. Li, Z. Chen, Compounds, Designed synthesis of LaCoO₃/N-doped reduced graphene oxide nanohybrid as an efficient bifunctional electrocatalyst for ORR and OER in alkaline medium, *J. Alloy. Compd.* 725 (2017) 260–269.
- [62] K. Zhang, R. Zou, Advanced transition metal-based OER electrocatalysts: current status, opportunities, and challenges, *Small* 17 (2021) 2100129.
- [63] D. Hassen, M. Shenashen, A. El-Safty, A. Elmarakbi, S. El-Safty, Anisotropic N-Graphene-diffused Co₃O₄ nanocrystals with dense upper-zone top-on-plane exposure facets as effective ORR electrocatalysts, *Sci. Rep.* 8 (2018) 1–14.
- [64] W. Yuan, Y. Wang, P. Chernev, K. Klingan, M. Reza Mohammadi, S. Loos, C. Pasquini, P. Kubella, S. Jiang, Z. Cui, S. Zhu, Z. Li, S. Wu, H. Dau, J. Zhang, Y. Liang, Tuning cobalt eg occupation of Co-NCNT by manipulation of crystallinity facilitates more efficient oxygen evolution and reduction, *J. Catal.* 383 (2020) 221–229.
- [65] M. Fronzi, S.A. Tawfik, C. Stampfl, M. Ford, Magnetic properties of stoichiometric and defective Co₉S₈, *Phys. Chem. Chem. Phys.* 20 (2018) 2356–2362.
- [66] F. Bai, X. Qu, J. Wang, X. Chen, W. Yang, Interfaces, confinement catalyst of Co₉S₈@N-doped carbon derived from intercalated Co(OH)₂ precursor and enhanced electrocatalytic oxygen reduction performance, *ACS Appl. Mater. Interfaces* 12 (2020) 33740–33750.
- [67] C. Zhao, X. Dai, T. Yao, W. Chen, X. Wang, J. Wang, J. Yang, S. Wei, Y. Wu, Y. Li, Ionic exchange of metal-organic frameworks to access single nickel sites for efficient electroreduction of CO₂, *J. Am. Chem. Soc.* 139 (2017) 8078–8081.
- [68] H. Gao, S. Zhu, Y. Kang, D.A. Dinh, K.S. Hui, F. Bin, X. Fan, F. Chen, A. Mahmood, J. Geng, Zeolitic imidazolate framework-derived Co-Fe@NC for rechargeable hybrid sodium-air battery with a low voltage gap and long cycle life, *ACS Appl. Energy Mater.* 5 (2022) 1662–1671.
- [69] W. Gu, Y. Song, J. Liu, F. Wang, Lanthanum-based compounds: electronic band-gap-dependent electrocatalytic materials for oxygen reduction reaction, *Chem. Eur. J.* 23 (2017) 10126–10132.
- [70] Z. Chen, Y. Song, J. Cai, X. Zheng, D. Han, Y. Wu, Y. Zang, S. Niu, Y. Liu, J. Zhu, Tailoring the d-band centers enables Co₄N nanosheets to be highly active for hydrogen evolution catalysis, *Angew. Chem.* 57 (2018) 5170–5174.

- [71] Q. Song, J. Li, S. Wang, J. Liu, X. Liu, L. Pang, H. Li, H. Liu, Enhanced electrocatalytic performance through body enrichment of co-based bimetallic nanoparticles in situ embedded porous N-doped carbon spheres, *Small* 15 (2019) 1903395.
- [72] Y. Yan, Z. Zhao, J. Zhao, Y. Xu, Y. Xu, Y. Zhao, W. Tang, J. Lee, Ultrathin CuNi nanosheets for CO₂ reduction and O₂ reduction reaction in fuel cells, *ACS Mater. Lett.* 3 (2021) 1143–1150.
- [73] J. Suntivich, K.J. May, H.A. Gasteiger, J.B. Goodenough, Y. Shao-Horn, A perovskite oxide optimized for oxygen evolution catalysis from molecular orbital principles, *Science* 334 (2011) 1383–1385.
- [74] J. Suntivich, H.A. Gasteiger, N. Yabuuchi, H. Nakanishi, J.B. Goodenough, Y. Shao-Horn, Design principles for oxygen-reduction activity on perovskite oxide catalysts for fuel cells and metal-air batteries, *Nat. Chem.* 3 (2011) 546–550.
- [75] Y. Sun, H. Liao, J. Wang, B. Chen, S. Sun, S.J.H. Ong, S. Xi, C. Diao, Y. Du, J. O. Wang, Covalency competition dominates the water oxidation structure–activity relationship on spinel oxides, *Nat. Catal.* 3 (2020) 554–563.
- [76] Y. Pan, K. Sun, Y. Lin, X. Cao, Y. Cheng, S. Liu, L. Zeng, W.C. Cheong, D. Zhao, K. Wu, Electronic structure and d-band center control engineering over M-doped CoP (M = Ni, Mn, Fe) hollow polyhedron frames for boosting hydrogen production, *Nano Energy* 56 (2019) 411–419.
- [77] J. Hwang, R.R. Rao, L. Giordano, Y. Katayama, Y. Yu, Y. Shao-Horn, Perovskites in catalysis and electrocatalysis, *Science* 358 (2017) 751–756.
- [78] M. Sharma, J.H. Jang, D.Y. Shin, J.A. Kwon, D.H. Lim, D. Choi, H. Sung, J. Jang, S. Y. Lee, K. Lee, E. Science, Work function-tailored graphene via transition metal encapsulation as a highly active and durable catalyst for the oxygen reduction reaction, *Energy Environ. Sci.* 12 (2019) 2200–2211.
- [79] Z. Chen, L. Cai, X. Yang, C. Kronawitter, L. Guo, S. Shen, B. Koel, Reversible structural evolution of NiCoO_xH_y during the oxygen evolution reaction and identification of the catalytically active phase, *ACS Catal.* 8 (2018) 1238–1247.
- [80] H. Hu, B.Y. Guan, X. Lou, Construction of complex CoS hollow structures with enhanced electrochemical properties for hybrid supercapacitors, *Chem* 1 (2016) 102–113.
- [81] Y. Zhu, T.R. Kuo, Y.H. Li, M.Y. Qi, G. Chen, J. Wang, Y.J. Xu, H. Chen, Emerging dynamic structure of electrocatalysts unveiled by in situ X-ray diffraction/absorption spectroscopy, *Energy Environ. Sci.* 14 (2021) 1928–1958.
- [82] C.N. Brodsky, R.G. Hadt, D. Hayes, B.J. Reinhart, N. Li, L.X. Chen, D. Nocera, In situ characterization of cofacial Co (IV) centers in Co₄O₄ cubane: Modeling the high-valent active site in oxygen-evolving catalysts, *Proc. Natl. Acad. Sci. U.S.A.* 114 (2017) 3855–3860.
- [83] Y. Li, G. Chen, Y. Zhu, Z. Hu, T.S. Chan, S. She, J. Dai, W. Zhou, Z. Shao, Activating both basal plane and edge sites of layered cobalt oxides for boosted water oxidation, *Adv. Funct. Mater.* 31 (2021) 2103569.
- [84] C. Ye, J. Liu, Q. Zhang, X. Jin, Y. Zhao, Z. Pan, G. Chen, Y. Qiu, D. Ye, L. Gu, Activating metal oxides nanocatalysts for electrocatalytic water oxidation by quenching-induced near-surface metal atom functionality, *J. Am. Chem. Soc.* 143 (2021) 14169–14177.
- [85] L. Reith, C.A. Triana, F. Pazoki, M. Amiri, M. Nyman, G. Patzke, Unraveling nanoscale cobalt oxide catalysts for the oxygen evolution reaction: maximum performance, minimum effort, *J. Am. Chem. Soc.* 143 (2021) 15022–15038.
- [86] Y.J. Li, L. Cui, P.F. Da, K.W. Qiu, W.J. Qin, W.B. Hu, X.W. Du, K. Davey, T. Ling, S. Qiao, Multiscale structural engineering of Ni-doped CoO nanosheets for zinc-air batteries with high power density, *Adv. Mater.* 30 (2018) 1804653.